



HAL
open science

Visible light optical coherence correlation spectroscopy

Stephane Broillet, Daniel Szlag, Arno Bouwens, Lionel Maurizi, Heinrich Hofmann, Theo Lasser, Marcel Leutenegger

► **To cite this version:**

Stephane Broillet, Daniel Szlag, Arno Bouwens, Lionel Maurizi, Heinrich Hofmann, et al.. Visible light optical coherence correlation spectroscopy. *Optics Express*, 2014, 22 (18), pp.21944. 10.1364/OE.22.021944 . hal-02163430

HAL Id: hal-02163430

<https://hal.science/hal-02163430v1>

Submitted on 9 Mar 2021

HAL is a multi-disciplinary open access archive for the deposit and dissemination of scientific research documents, whether they are published or not. The documents may come from teaching and research institutions in France or abroad, or from public or private research centers.

L'archive ouverte pluridisciplinaire **HAL**, est destinée au dépôt et à la diffusion de documents scientifiques de niveau recherche, publiés ou non, émanant des établissements d'enseignement et de recherche français ou étrangers, des laboratoires publics ou privés.

Visible light optical coherence correlation spectroscopy

Stephane Broillet,^{1*} Daniel Szlag,¹ Arno Bouwens,¹ Lionel Maurizi,²
Heinrich Hofmann,² Theo Lasser,¹ and Marcel Leutenegger¹

¹Laboratoire d'Optique Biomédicale LOB, École Polytechnique Fédérale de Lausanne,
CH-1015 Lausanne, Switzerland

²Laboratory of Powder Technology LTP, École Polytechnique Fédérale de Lausanne,
CH-1015 Lausanne, Switzerland

*stephane.broillet@epfl.ch

Abstract: Optical coherence correlation spectroscopy (OCCS) allows studying kinetic processes at the single particle level using the backscattered light of nanoparticles. We extend the possibilities of this technique by increasing its signal-to-noise ratio by a factor of more than 25 and by generalizing the method to solutions containing multiple nanoparticle species. We applied these improvements by measuring protein adsorption and formation of a protein monolayer on superparamagnetic iron oxide nanoparticles under physiological conditions.

© 2014 Optical Society of America

OCIS codes: (290.5850) Scattering, particles; (030.1670) Coherent optical effects; (170.0170) Medical optics and biotechnology; (170.4500) Optical coherence tomography.

References and links

1. P. Ghosh, G. Han, M. De, C. Kim, and V. Rotello, "Gold nanoparticles in delivery applications," *Adv. Drug Delivery Rev.* **60**, 1307–1315 (2008).
2. H. Jans and Q. Huo, "Gold nanoparticle-enabled biological and chemical detection and analysis," *Chem. Soc. Rev.* **41**, 2849–2866 (2012).
3. A. Gupta, R. Naregalkar, V. Vaidya, and M. Gupta, "Recent advances on surface engineering of magnetic iron oxide nanoparticles and their biomedical applications," *Nanomedicine* **2**, 23–39 (2007).
4. Q. Pankhurst, N. Thanh, S. Jones, and J. Dobson, "Progress in applications of magnetic nanoparticles in biomedicine," *J. Phys. D: Appl. Phys.* **42**, 1–15 (2009).
5. R. Singh and H. Nalwa, "Medical applications of nanoparticles in biological imaging, cell labeling, antimicrobial agents, and anticancer nanodrugs," *J. Biomed. Nanotechnol.* **7**, 489–503 (2011).
6. S. Broillet, A. Sato, S. Geissbuehler, C. Pache, A. Bouwens, T. Lasser, and M. Leutenegger, "Optical coherence correlation spectroscopy (occs)," *Opt. Express* **22**, 782–802 (2014).
7. J. Robinson, T. Takizawa, D. Vandré, and R. Burry, "Ultrasmall immunogold particles: Important probes for immunocytochemistry," *Microsc. Res. Tech.* **42**, 13–23 (1998).
8. K. Huang, H. Ma, J. Liu, S. Huo, A. Kumar, T. Wei, X. Zhang, S. Jin, Y. Gan, P. Wang, S. He, X. Zhang, and X.-J. Liang, "Size-dependent localization and penetration of ultrasmall gold nanoparticles in cancer cells, multicellular spheroids, and tumors in vivo," *ACS Nano* **6**, 4483–4493 (2012).
9. T. Cedervall, I. Lynch, S. Lindman, T. Berggard, E. Thulin, H. Nilsson, K. Dawson, and S. Linse, "Understanding the nanoparticle-protein corona using methods to quantify exchange rates and affinities of proteins for nanoparticles," *Proc. Natl. Acad. Sci. U. S. A.* **104**, 2050–2055 (2007).
10. U. Sakulkhu, M. Mahmoudi, L. Maurizi, J. Salaklang, and H. Hofmann, "Protein corona composition of superparamagnetic iron oxide nanoparticles with various physico-chemical properties and coatings," *Sci. Rep.* **4**, 1–9 (2014).
11. P. Aggarwal, J. Hall, C. McLeland, M. Dobrovolskaia, and S. McNeil, "Nanoparticle interaction with plasma proteins as it relates to particle biodistribution, biocompatibility and therapeutic efficacy," *Adv. Drug Delivery Rev.* **61**, 428–437 (2009).

12. C. Walkey and W. Chan, "Understanding and controlling the interaction of nanomaterials with proteins in a physiological environment," *Chem. Soc. Rev.* **41**, 2780–2799 (2012).
13. C. Rucker, M. Potzl, F. Zhang, W. Parak, and G. Nienhaus, "A quantitative fluorescence study of protein monolayer formation on colloidal nanoparticles," *Nat. Nanotechnol.* **4**, 577–580 (2009).
14. S. Dominguez-Medina, S. McDonough, P. Swanglap, C. Landes, and S. Link, "In situ measurement of bovine serum albumin interaction with gold nanospheres," *Langmuir* **28**, 9131–9139 (2012).
15. I. Kohli, S. Alam, B. Patel, and A. Mukhopadhyay, "Interaction and diffusion of gold nanoparticles in bovine serum albumin solutions," *Appl. Phys. Lett.* **102**, 203705 (2013).
16. M. Mikhaylova, D. Kim, C. Berry, A. Zagorodni, M. Toprak, A. Curtis, and M. Muhammed, "Bsa immobilization on amine-functionalized superparamagnetic iron oxide nanoparticles," *Chem. Mater.* **16**, 2344–2354 (2004).
17. Z. Wang, T. Yue, Y. Yuan, R. Cai, C. Niu, and C. Guo, "Kinetics of adsorption of bovine serum albumin on magnetic carboxymethyl chitosan nanoparticles," *Int. J. Biol. Macromol.* **58**, 57–65 (2013).
18. M. Villiger and T. Lasser, "Image formation and tomogram reconstruction in optical coherence microscopy," *J. Opt. Soc. Am. A* **27**, 2216–2228 (2010).
19. R. A. Leitgeb, M. Villiger, A. H. Bachmann, L. Steinmann, and T. Lasser, "Extended focus depth for fourier domain optical coherence microscopy," *Opt. Lett.* **31**, 2450–2452 (2006).
20. C. Pache, N. Bocchio, A. Bouwens, M. Villiger, C. Berclaz, J. Goulley, M. Gibson, C. Santschi, and T. Lasser, "Fast three-dimensional imaging of gold nanoparticles in living cells with photothermal optical lock-in optical coherence microscopy," *Opt. Express* **20**, 21385–21399 (2012).
21. M. Villiger, C. Pache, and T. Lasser, "Dark-field optical coherence microscopy," *Opt. Lett.* **35**, 3489–3491 (2010).
22. J. Izatt and M. Choma, *Optical Coherence Tomography: Technology and Applications* (Springer Verlag, Berlin, 2008).
23. M. Wojtkowski, V. Srinivasan, T. Ko, J. Fujimoto, A. Kowalczyk, and J. Duker, "Ultrahigh-resolution, high-speed, fourier domain optical coherence tomography and methods for dispersion compensation," *Opt. Express* **12**, 2404–2422 (2004).
24. C. Dorrer, N. Belabas, J.-P. Likforman, and M. Joffre, "Spectral resolution and sampling issues in fourier-transform spectral interferometry," *J. Opt. Soc. Am. B* **17**, 1795–1802 (2000).
25. T. Wohland, R. Rigler, and H. Vogel, "The standard deviation in fluorescence correlation spectroscopy," *Biophys. J.* **80**, 2987–2999 (2001).
26. N. L. Thompson, *Fluorescence correlation spectroscopy. In: Topics in Fluorescence Spectroscopy*, vol. 1 (Plenum Press, 1991).
27. U. Meseth, T. Wohland, R. Rigler, and H. Vogel, "Resolution of fluorescence correlation measurements," *Biophys. J.* **76**, 1619–1631 (1999).
28. B. Berne and R. Pecora, *Dynamic Light Scattering with Applications to Chemistry, Biology and Physics. Chapter 5: Model Systems of Spherical Molecules* (John Wiley and Sons, 1976).
29. M. Leutenegger, R. Rao, R. Leitgeb, and T. Lasser, "Fast focus field calculations," *Opt. Express* **14**, 11277–11291 (2006).
30. R. Leitgeb, C. Hitzenberger, and A. Fercher, "Performance of fourier domain vs. time domain optical coherence tomography," *Opt. Express* **11**, 889–894 (2003).
31. M. Chastellain, A. Petri, and H. Hofmann, "Particle size investigations of a multistep synthesis of pva coated superparamagnetic nanoparticles," *J. Colloid Interface Sci.* **278**, 353–360 (2004).
32. L. Maurizi, U. Sakulku, L. Crowe, V. Dao, N. Leclaire, J.-P. Vallee, and H. Hofmann, "Syntheses of cross-linked polymeric superparamagnetic beads with tunable properties," *RSC Adv.* **4**, 11142–11146 (2014).
33. M. Ferrer, R. Duchowicz, B. Carrasco, J. De La Torre, and A. Acuna, "The conformation of serum albumin in solution: A combined phosphorescence depolarization-hydrodynamic modeling study," *Biophys. J.* **80**, 2422–2430 (2001).
34. H. Kenneth Walker, W. Dallas Hall, and J. Willis Hurst, *Clinical Methods, 3rd edition; The History, Physical, and Laboratory Examinations; Chapter 101: Serum Albumin and Globulin* (Butterworths, 1990).

1. Introduction

Nanoparticles (NPs) are studied thoroughly for applications in medicine and life sciences: of special interest are gold NPs due to their optical, chemical, and biocompatible properties [1, 2] and superparamagnetic iron oxide nanoparticles (SPIONs) [3–5]. Recently, we have shown that optical coherence correlation spectroscopy (OCCS) can measure the diffusion coefficient of gold NPs down to diameters of 30 nm with near-infrared light [6]. There are advantages to use even smaller gold NPs because of an enhanced labeling efficiency [7] and improved penetration into biological samples [8], showing the importance of measuring the dynamics of smaller gold NPs.

Another very interesting feature would be to have the possibility to distinguish different species of scattering NPs, for instance based on their size. This would give the possibility to distinctively label several targets in measurements and to measure chemical reaction kinetics, for instance.

The coating process of nanoparticles (NPs) with biomolecules generates a so-called protein corona [9, 10]. Understanding the properties of this coating is important for the application of NPs in living organisms [11]. Most strategies involve the removal of the NP–protein complex from their original physiological environment [12]. A complementary approach investigates the adsorption of proteins under physiological conditions. So far, the adsorption of either bovine serum albumin (BSA) or human serum albumin (HSA) has been studied with different types of NPs using fluorescence correlation spectroscopy (FCS), as for example the coating process of FePt NPs and quantum dots [13] or gold NPs [14, 15]. Adsorption of BSA on SPIONs has already been studied [16, 17], however, a quantitative analysis of their diffusion properties in physiological conditions has not been performed yet.

OCCS exploits the backscattered light of NPs illuminated by a broadband light source, giving simultaneous access to several sampling volumes along the optical axis. Over a large concentration range, this technique allows the extraction of the diffusion coefficient and concentration of NPs using an auto-correlation analysis. In this work we greatly extend the application potential of OCCS by shifting the OCCS instrument from the near-infrared to the visible wavelength range. The signal-to-noise ratio (SNR) has been increased by a factor of more than 25 due to a much increased NA allowing the extraction of the diffusion coefficient of gold NPs down to a size of 10 nm diameter. In addition, the auto-correlation model has been generalized to solutions hosting multiple NP species and this generalized model is used to retrieve the particle fractions in a mixture of two NP species. Using our novel OCCS technique, we show its application to the study of BSA adsorption on SPIONs by measuring their hydrodynamic radius under physiological conditions. This combines the advantages of not having to use fluorescent labels (thus preventing the risk that these labels change the properties of the NPs) and of avoiding additional separation steps to remove unbound protein from the solution.

2. Materials and methods

2.1. Low coherence interferometer

Figure 1 depicts the OCCS instrument which is based on a Mach-Zehnder interferometer [6, 18–21]. This visible light OCCS instrument is based on low coherence interferometric principles as described in [6]. The light from a super-continuum source (Koheras SuperK Extreme, NKT Photonics) is spectrally filtered to obtain a broad visible spectrum centered at 590 nm wavelength with a bandwidth of 160 nm full width at half-maximum (FWHM). The light is linearly polarized by a polarizing beam splitter and delivered to the interferometer by a single-mode fiber (mode field diameter of 3.4 μm , Fibercore). After collimation, the light is split into a reference beam and an illumination beam by a non-polarizing 50:50 beam splitter. The reference beam passes through glass prisms with variable thicknesses for compensating the dispersion difference in the illumination and sample arms. The illumination beam passes through an axicon lens (176° cone angle, Asphericon) generating a Bessel beam, which is further imaged by a 300 mm achromatic lens and an apochromatic water immersion objective (40 \times , NA 1.15, Olympus) into the sample at the focal plane of the objective. The power impinging on the sample is adjusted between 2–10 mW, depending on the experiment. The annular mask F_{ill} blocks residual stray light from the tip of the axicon. The back-scattered sample field is collected by the objective, superimposed with the reference field and focused into a single-mode fiber (mode field diameter of 3.4 μm , Thorlabs). The fiber guides the collected field to the customized spectrometer (transmission grating; 600 lines/mm, Wasatch) for the registration

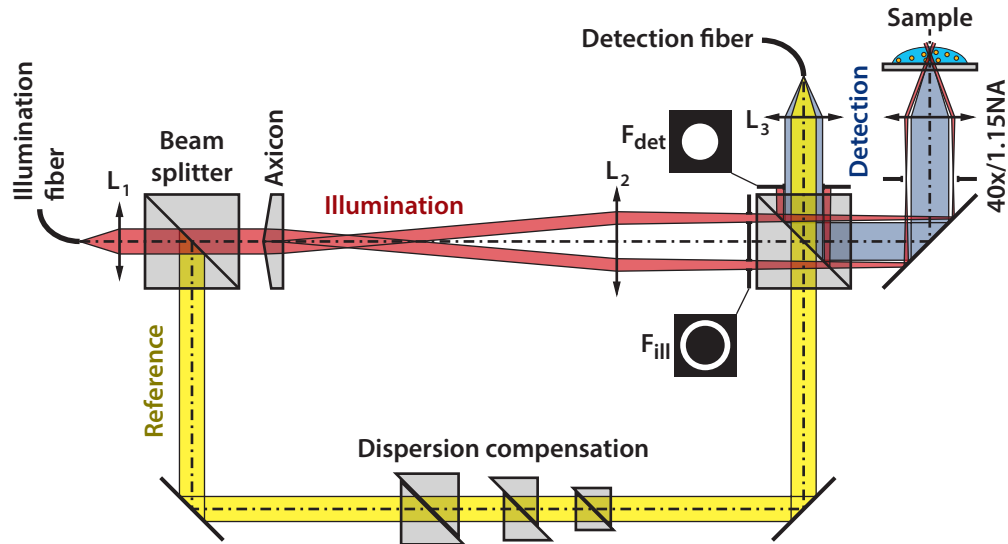


Fig. 1. Visible light OCCS interferometer with a Bessel-Gauss configuration [18]. The axicon generates a Bessel beam illumination, whereas the detection mode is Gaussian. The apertures F_{ill} and F_{det} provide a dark field contrast [21].

of the spectral interferogram from 420 nm to 760 nm wavelength (linear CMOS array Sprint spL2048-140km with 2048 pixels, Basler).

As illustrated in Fig. 1, the illumination and detection beams do not overlap in the aperture plane of the objective: any specular reflected light from the glass slide is blocked by the diaphragm F_{det} . The interferometer was conceived with a minimum number of optical elements in order to increase the detection efficiency and to simplify the alignment of components. Because the glass slide is always closer to the objective than the sample, a dark field is obtained even though the filters F_{ill} and F_{det} are not placed in a pupil plane but just as close to the objective as possible. The dark field contrast is essential for a high SNR while detecting the weak back-scattered field from the NPs. This interferometer implements a Bessel illumination and Gaussian detection configuration [18]. The illumination field corresponds to a radial zero-order Bessel distribution in the focal plane with the first minimum located at $0.22 \mu\text{m}$ lateral radius, whereas the detection mode is Gaussian with an effective numerical aperture (NA) close to 0.9.

In typical experiments the detector was driven at a line rate of 20 kHz with an exposure time of $48 \mu\text{s}$. The reference arm intensity was adjusted to about 75% of the available dynamic range of the camera. By taking the Fourier transform of the spectrum (resampled at equidistant wave numbers, λ to k mapping), we obtain the time-dependent signal traces extending over several sampling volumes [22]. Here, the background corrected depth profile containing a sequence of sampling volumes (center to center distance of $0.35 \mu\text{m}$ in water) was then extracted by using an algorithm based on the discrete Fourier transform (DFT). The signal processing leading to the time-dependent signal traces is indicated in Fig. 2. An integration kernel to get the tomogram from the sample spectrum by a matrix product was calculated such that (i) it resampled the spectrum at equidistant wave numbers (λ to k mapping); (ii) it compensated the residual dispersion $\phi(k)$ by multiplying the spectrum with calibrated phase factors $\exp(i\phi(k))$ calculated with an automatic numerical iterative procedure developed by Wojtkowski et al. [23]; and (iii) Fourier transformed the corrected spectrum to yield the tomogram in (iv) the region of interest.

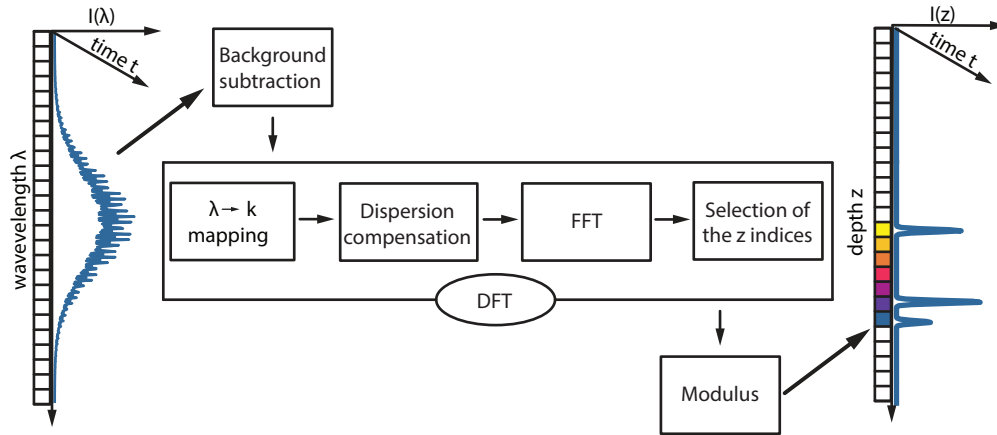


Fig. 2. Signal processing leading to the time-dependent signal traces. The interference signal is recorded via a spectrometer. The average spectrum is then subtracted from the recorded signal (background subtraction). The new DFT integration kernel replaces the following steps: (i) λ to k mapping; (ii) dispersion compensation; (iii) fast Fourier transform of the spectrum; and (iv) selection of the sampling volumes of interest. The modulus of the signal is taken to yield the time-dependent signal traces.

Thereby, the matrix multiplication of this kernel with the measured spectra directly yielded the depth profiles. This algorithm is only performed on the sampling volumes in the optical focal area in order to minimize the calculation time. In all the calculations that follow, 150 sampling volumes are calculated. Auto-correlations of the absolute values of these time-dependent signals were then calculated. In this application, the new DFT algorithm is about six times faster than the previous FFT algorithm [6].

In detail, the DFT kernel \mathbf{F} is an $M \times N$ matrix, where M is the number of tomogram samples $m \in [0, N)$ and N is the number of interferogram samples. The tomogram is obtained as matrix product $I(z) = \mathbf{F} \cdot I(\lambda)$. In other words, $I(z_m) = \sum_{n=0}^{N-1} F_{mn} I(\lambda_n)$, where $z_m = m\Delta z = m \cdot 0.35 \mu\text{m}$. The fast Fourier transform is performed by $F_{mn} = \exp(-2i\pi mn/N)$ for $m, n \in \{0, N-1\}$.

In the DFT algorithm, the dispersion is compensated by multiplying the interferogram samples with a factor $f_n = \exp(i\phi(\lambda_n))$. An extra amplitude component would allow reshaping the spectral amplitudes. Therefore, the kernel implementing steps (ii–iv) writes as $F_{mn} = f_n \exp(-2i\pi mn/N)$. The λ to k mapping (i) is performed by multiplying this kernel with an $N \times N$ identity matrix resampled at wavelengths corresponding to equidistant wave number samples. A high-quality resampling is achieved by Fourier-upsampling the columns of the identity matrix to yield $L \gtrsim 3N$ samples, which are then linearly interpolated at the desired wavelengths [24].

2.2. Sample preparation

Sample solutions of monodisperse polystyrene microspheres (PS MSs) with a diameter of 109 nm (POLYBEAD Microspheres 109 nm, Polysciences) and gold colloids (gold NPs) with diameters of 10, 15, 20, 30, 40 and 50 nm (EM.GC10, EM.GC15, EM.GC20, EM.GC30, EM.GC40, EM.GC50, British Biocell International) were used. To obtain the nominal concentrations, the solutions were prepared by diluting an adequate volume of stock solution in ultrapure water or in glycerol. All OCCS measurements were performed in plastic wells (μ -Slide 8 well, uncoated, sterile, Ibidi) with a well volume of 300 μl .

2.3. Correlation analysis of multiple components mixtures

The signal acquisition in OCCS and its auto-correlation analysis for single species was described in previous work [6], where the interested reader finds the detailed derivation of Eq. (1). The auto-correlation analysis of the OCCS signal $I_m(t)$ in a sampling volume m was subdivided into three distinct regimes depending on the number of particles in the sampling volume of interest N : the single particle ($N \ll 1$), the few particles ($N \sim 1$) and the many particles ($N \gg 1$) regimes. The general case is the few particles regime, which takes into account the diffusion of particles in and out of the sampling volume and a dynamic light scattering (DLS) contribution depending on the number of particles N in the sampling volume. In the few particles regime, the OCCS autocorrelation function can be written as

$$G_{F,m}(\tau) = \frac{\gamma}{N} \left[\left(1 + \frac{\tau}{\tau_{xy}} \right) \sqrt{1 + \frac{\tau}{\tau_z}} \right]^{-1} \left(1 + A_b \exp\left(-\frac{\tau}{\tau_b}\right) \right) \left(1 + N \exp\left(-\frac{\tau}{\tau_c}\right) \right), \quad (1)$$

where γ is the volume contrast [25] and N the average number of particles in the sampling volume. $\tau_{xy} = r_0^2(4D)^{-1}$ and $\tau_z = z_0^2(4D)^{-1}$ are the lateral and axial diffusion times, where D is the diffusion coefficient, and r_0 and z_0 are the lateral and axial e^{-2} radii of an equivalent three-dimensional Gaussian volume. The exponential decay $\tau_b = r_b^2(4D)^{-1}$ with the characteristic length r_b and amplitude parameter A_b account for the Bessel profile. The last factor is the coherent contribution caused by speckle fluctuations of the back-scattered field of the NPs in one sampling volume. This coherent contribution is characterized by the decorrelation time $\tau_c = (8n^2k_0^2D)^{-1}$ known from dynamic light scattering (DLS), where n is the refractive index of the medium and k_0 is the central wave number of the source spectrum.

Here we extend this initial model to the study of multiple independently diffusing species i with different diffusion coefficients. Without the coherent contribution, Eq. (1) describes a correlation function for a signal similar to the intensity fluctuations in FCS. Therefore, we can apply the multi-species model derived for FCS, see for instance Thompson [26] and Meseth et al. [27]. For the coherent contribution, Berne and Pecora [28] describe a multi-species model in the context of DLS. In both cases, the multi-species models are linear combinations of the single-species correlation functions. Therefore, we can write the multi-species auto-correlation function as

$$G_{F,m}^{\text{mix}}(\tau) = \gamma \left(1 - \frac{\langle B \rangle}{\langle I_m \rangle} \right)^2 \frac{\sum N_i Q_i^2 D_{F,m,i}(\tau)}{(\sum N_i Q_i)^2}, \quad (2)$$

where

$$D_{F,m,i}(\tau) = \left[\left(1 + \frac{\tau}{\tau_{xy,i}} \right) \sqrt{1 + \frac{\tau}{\tau_{z,i}}} \right]^{-1} \left(1 + A_b \exp\left(-\frac{\tau}{\tau_{b,i}}\right) \right) \left(1 + N_i \exp\left(-\frac{\tau}{\tau_{c,i}}\right) \right). \quad (3)$$

$\langle I_m \rangle = \langle B \rangle + \sum N_i Q_i$ is the average signal in the sampling volume m and $\langle B \rangle$ is the average background. N_i is the average number and Q_i is the brightness of particles of species i . Q_i is proportional to the absolute value of the particle's electric field reflectivity. The squared prefactor stands for the background influence on the correlation amplitude. The total number of particles is $N = \sum N_i$ and $P_i = N_i/N$ are the fractions of the species. Each species contributes to the correlation amplitude by its concentration times the squared brightness which limits the discrimination of species with significant brightness differences.

2.4. Sampling volume characterization

The determination of r_0 and z_0 is essential for an appropriate fit model requiring an accurate characterization of the OCCS sampling volumes. In analogy to the near-infrared light

OCCS procedures described in [6], we characterized the sampling volume by imaging individual $\varnothing 50$ nm gold NPs. The scattering particles were dispersed in an agarose gel with 0.3% weight/volume ratio. We scanned individual NPs using a three-axis piezoscanning stage in the x-y plane (repeatability 0.01 μm , Physik Instrumente) while illuminating with a power of 5 mW. We compared the brightness profile measurements with ab initio calculations at the cen-

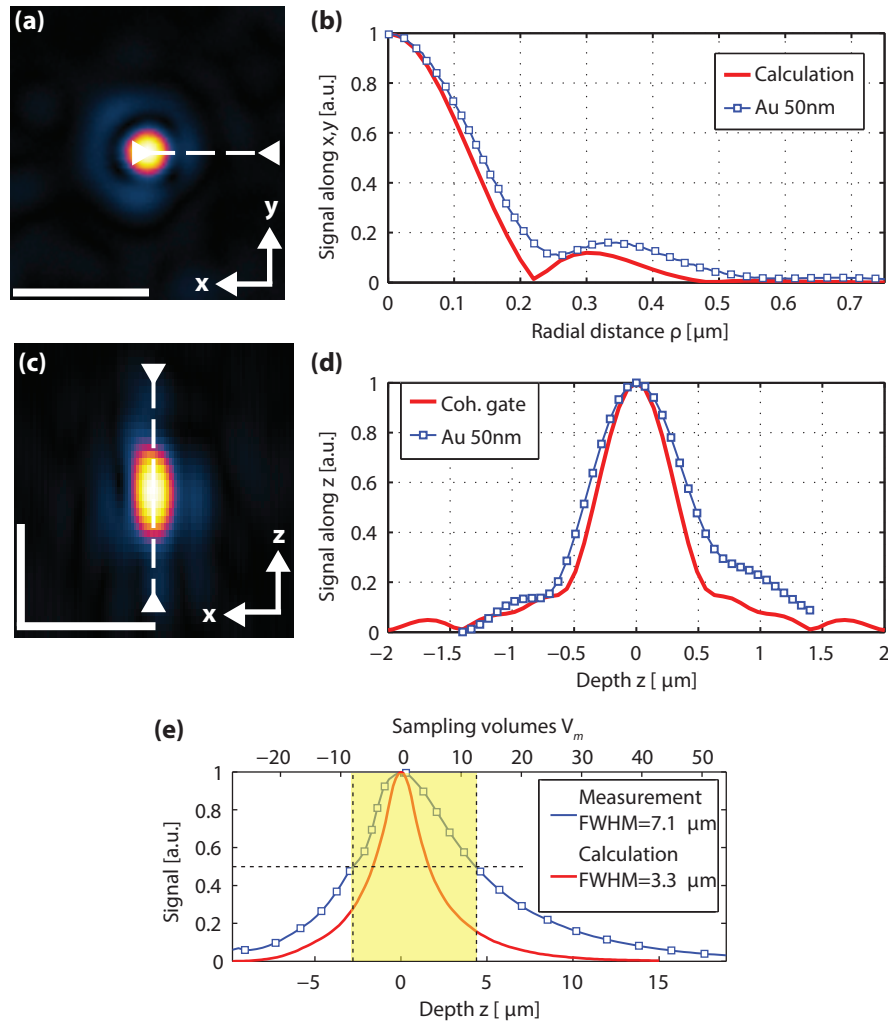


Fig. 3. Brightness profiles characterization. (a,c) Brightness profile cross-sections xy and xz measured with a $\varnothing 50$ nm single gold NP. Scalebars: 1 μm . (b,d) Average radial $\rho = \sqrt{x^2 + y^2}$ and axial (z) brightness profiles measured on ten $\varnothing 50$ nm gold NPs in comparison with calculations. (e) Depth of field characterization with $\varnothing 109$ nm PS MSs freely diffusing in water (concentration: 330 pM; illumination power: 5 mW; average on 10 measurements of 50 seconds). The useful DOF is indicated by the dashed lines showing the measured FWHM. V_0 corresponds to the focal sampling volume. The calculations in (b) and (e) were performed using the focus field calculation framework by Leutenegger et al. [29]. The coherence gate in (d) is calculated from the measured source spectrum $S(k)$ using the Wiener-Khinchine relation.

tral wavelength using the focus field calculation framework by Leutenegger et al. [29]. The brightness profile is rotationally symmetric around the optical axis z . Figures 3(a)–3(d) show the measured brightness profile $W(\mathbf{r})$. Figure 3(b) shows the measured radial brightness profiles $W(\mathbf{r})$ compared with the calculation performed at the central wavelength of 590 nm. We attribute the non-zero minimum (10% of the maximal signal) and larger profile in the measurement to the large illumination bandwidth and to the finite size of the NPs used. Figure 3(d) shows the measured axial brightness profiles $W(\mathbf{r})$ compared with the coherence gate determined by the measured source spectrum $S(k)$ and calculated using the Wiener-Khintchine relation. The e^{-2} half width z_0 of this calculated axial coherence gate is $0.95 \mu\text{m}$. There is a good agreement between the calculation and the measurement in the profiles' FWHM. The difference in the tail is $< 15\%$ of the maximal signal and is due to residual dispersion difference between the reference path and the illumination plus detection paths.

The depth of field (DOF) assessment is important for the evaluation of the number of useful sampling volumes along the optical axis. For assessing this parameter, we used a solution of $\varnothing 109 \text{ nm}$ PS MSs (concentration of 330 pM) freely diffusing in water, an illumination power of 5 mW and measured the time-averaged signal amplitude $\langle I_m \rangle$ for the sampling volumes V_m along the optical axis. Figure 3(e) compares the DOF (average over 10 measurements during 50 seconds) with our ab initio calculations. The measurements indicate a DOF of approximately $7 \mu\text{m}$ FWHM corresponding to 20 sampling volumes, which can be observed simultaneously in axial separation steps of $\Delta z = 0.35 \mu\text{m}$. The significant increase in DOF as compared to calculations is most likely caused by longitudinal chromatic aberrations in the illumination and detection paths.

2.5. Data Analysis

Care should be taken to carefully calibrate several parameters summarized in Table 1. Figure 3(d) confirms the good agreement between the calculated and the measured axial brightness profile. Therefore, the axial extent z_0 was extracted from the coherence length given by the spectrum of the light source in Fig. 3(d). The volume contrast factor γ was calculated from the measured PSF [25]. The lengths r_0 , r_b and the parameter A_b were calibrated for each sampling volume with an auto-correlation measurement of $\varnothing 109 \text{ nm}$ PS MSs matched to Eq. (1) by using the theoretical value for the diffusion coefficient D (concentration of 330 pM ; illumination power of 5 mW ; 10 measurements of 50 seconds). This calibration was repeated for every measurement session. The characteristic lengths r_0 , r_b , z_0 as well as the parameters A_b and γ were then kept fixed and Eq. (1) was used to fit the auto-correlations shown in Fig. 5(a) and Fig. 7(a), where only N and D have been retained as free fit parameters. The hydrodynamic radii R_H of particles in Fig. 7(b) and Fig. 7(c) were calculated using the Stokes-Einstein relation $D = k_B T / (3\pi\eta 2R_H)$, where k_B is the Boltzmann constant, T the absolute temperature (295 K), and η the fluid viscosity.

Table 1. Typical values of the calibrated fit parameters for the focal sampling V_0 .

Parameter	z_0	r_0	r_b	A_b	γ
Value	$0.95 \mu\text{m}$	$0.49 \mu\text{m}$	$0.17 \mu\text{m}$	0.37	0.25
Standard deviation	$0.04 \mu\text{m}$	$0.06 \mu\text{m}$	$0.03 \mu\text{m}$	0.09	0.04

At the single particle level, scaling γ promotes linearly to N . With increasing concentration the coherent contribution becomes significant and the influence of γ on N diminishes. Scaling all three characteristic lengths by ε scales D by ε^2 . Independent errors in the characteristics lengths and/or the parameter A_b may lead to errors in D and/or N , but certainly worsen the fit

quality because the shape of the model correlation function differs from the measurement.

For the two-species mixture measurements, the same procedure is first applied to solutions of single species to extract also the diffusion coefficients D_1 and D_2 . In order to calculate the relative brightness of the two species, the average signal $\langle I_0 \rangle$ in the focal volume (V_0 in Fig. 3(e)) averaged on 10 measurements of 20 seconds is calculated (same conditions for the two species: concentration of 150 pM; illumination power of 5 mW). The brightness was then estimated by subtracting the background: $Q = \langle I_0 \rangle - \langle B \rangle$. The extracted parameters are then used for fitting the auto-correlations shown in Fig. 6(a) using Eq. (2) with only N_1 and N_2 as free fit parameters.

Errors scaling the absolute concentrations N of all species equally do not affect the species fractions P . Errors scaling the diffusion constants D of all species equally also have little effect on P . However, erroneous shapes of the single-species correlation functions affect P because the fit will find a better match of the measured correlation function at an erroneous P . Hence, all errors in characteristic lengths and/or the parameters A_b and γ have little effect on P unless the shape of the model function changes. Obviously, an error in the relative brightness Q is critical as it affects the weights Q^2P and QP in Eq. (2).

3. Experimental results

3.1. Improvement of the signal-to-noise ratio

The OCCS interferometer contains a high NA objective to enhance the collection efficiency and a variable aperture F_{det} to adjust the NA of the detection mode. In order to demonstrate the improvement in signal detection, we characterized the SNR in function of the detection NA. Following Leitgeb et al. [30], the SNR in an optical coherence microscope is given as

$$SNR = \frac{\langle I_m^2 \rangle}{\sigma_N^2}, \quad (4)$$

where $\langle I_m \rangle$ is the signal amplitude in sampling volume V_m and σ_N^2 is the noise variance. The noise variance is evaluated by calculating the root mean square of a signal-free region within the tomogram at higher depths to avoid cover slip artifacts. This signal-free region may contain some background from multiply scattered light.

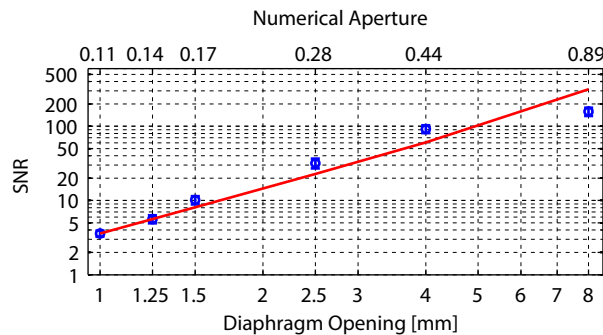


Fig. 4. SNR measurements with different diaphragm F_{det} settings and corresponding detection NA. The solid line starts at the SNR measured with 1mm opening and follows the increase of the solid detection angle.

We measured $\varnothing 109$ nm PS MSs diffusing freely in water with different diaphragm F_{det} openings (concentration of 330 pM; illumination power of 5 mW; 10 measurements during 50 seconds for every opening value; line rate of 20 kHz with an exposure time of 48 μ s). The SNR

was calculated with respect to the averaged signal $\langle I_0 \rangle$ in the sampling volume V_0 . The noise variance was calculated at V_{50} (17.5 μm from the center of V_0) well outside the DOF but close enough to the optical focus. Figure 4 shows the results of the measurements with respect to the F_{det} opening. The NA of the detection mode is calculated from this opening diameter. The diaphragm opening of 1.25 mm diameter corresponds to the near-infrared light OCCS described in [6]. The solid line represents the calculated solid angle seen by the detection fiber $\Omega = 2\pi [1 - \cos(\arcsin(\text{NA}/n))]$ normalized by the SNR at the smallest opening. The measured SNR improved proportionally with the solid detection angle Ω . At intermediate NA, the measured SNR was about twice the expected value, most likely due to a higher back-scattered signal at intermediate detection angles. In contrast, the SNR improved only slightly at high NA, which could be caused by residual spherical aberration becoming particularly marked at high NA. Due to the diaphragm opening increase to 8 mm, the SNR improved by a factor of up to $28\times$ as compared to the 1.25 mm diameter F_{det} used in [6].

3.2. Instrument validation with gold NPs

We validated this novel visible light OCCS instrument by measuring freely diffusing gold NPs with different NP diameters. Figure 5 summarizes the results of these experiments. The normalized auto-correlations in V_0 (see Fig. 3(e)) of differently sized gold NPs are shown in Fig. 5(a) (NPs concentrations: 150 pM except 35 pM for $\varnothing 50$ nm; 60 pM for $\varnothing 40$ nm. Illumination powers: 2 mW for $\varnothing 50$ nm; 5 mW for $\varnothing 40$ nm, $\varnothing 30$ nm; 10 mW for $\varnothing 20$ nm, $\varnothing 15$ nm, $\varnothing 10$ nm). These NPs were freely diffusing in glycerol/water solutions with 60% w/w of glycerol. The diffusion coefficients were extracted from the signal in the sampling volumes in the focal area from V_{-2} to V_2 independently and then averaged. These sampling volumes offered the best SNR and their small size allowed measurements at the few particles regime at the applied NPs concentrations. Extracting the diffusion coefficients was based on the fitting procedure described in the data analysis section. The fit residuals were small ($< 2\%$) for NPs diameters ≥ 20 nm but increasing for smaller NPs due to low SNR. The extracted diffusion coefficients in Fig. 5(b) are related by the Stokes-Einstein relation. The viscosity of the glycerol/water solutions was obtained by measuring $\varnothing 109$ nm PS MSs in this mixture. The deviation of the diffusion coefficient from the absolute theoretical values varies between 3.5% and 12% (smallest NPs). The improved SNR allows characterizing gold NPs of $\varnothing 10$ nm which is $3\times$ smaller than with the previous OCCS instrument [6]. Because the back-scattered field scales with the NP volume, this finding confirms an $\sim 27\times$ higher sensitivity.

3.3. Measurements of gold NPs/PS MSs mixtures

OCCS allowed measuring the fractions P_1 of gold NPs and P_2 of PS MSs in a two component solution. Figure 6 shows the results of freely diffusing $\varnothing 40$ nm gold NPs mixed with $\varnothing 109$ nm PS MSs. The normalized auto-correlations $G_{F,0}^{\text{mix}}(\tau)$ with varying fractions P_1 from 0% to 100% of $\varnothing 40$ nm gold NPs are shown in Fig. 6(b). The total particle concentration was kept constant at 150 pM and the host medium was pure water. The diffusion coefficient of each species was first extracted separately from the single species measurements using Eq. (1). For the fraction analysis, the $\varnothing 40$ nm gold NPs brightness was defined as $Q_1 = 1$ and a relative brightness $Q_2 = 0.86$ for the $\varnothing 109$ nm PS MSs was measured. A fit per sampling volume to the extended auto-correlation function $G_{F,m}^{\text{mix}}(\tau)$ (Eq. (2)) for the five sampling volumes V_{-2} to V_2 was used for extracting the fractions (see data analysis). The residuals of $< 4\%$ underline the quality of these fits. Figure 6(b) shows that the measured average fractions \overline{P}_1 increase linearly with the prepared fractions P_1 . The red line represents the theoretical values, while the dotted black line is the linear regression of the measured \overline{P}_1 . For the solutions with only one type of particles, fitting Eq. (2) for two species never totally removed the contribution for the other particle. Noise

and residual mismatches between the fit model and the measured auto-correlations caused the fit to find up to 8% of the other type of particles.

The measured fractions \bar{P}_1 had an uncertainty of $\approx 6\%$ and an absolute error $< \pm 8\%$. Varying the characteristic lengths and the parameter A_b within the mean values \pm the standard deviation given in Table 1 worsened neither the uncertainty nor the linearity significantly. However, the absolute errors at $P_1 = 0\%$ and 100% increased to $\pm 20\%$ in the worst case. In all cases, the two NPs species could be clearly distinguished.

3.4. Protein adsorption on SPIONs

We measured the adsorption of BSA onto SPIONs with OCCS. Naked SPIONs (maghemite phase of $8\text{ nm} \pm 2\text{ nm}$ crystallite's diameter) were preliminary coated with a mixture of polyvinyl alcohol (PVA) as described in previous works [31, 32] (these PVA-coated SPIONs will simply be called SPIONs for the remainder of this document). Their hydrodynamic radius R_H in a PBS buffer (phosphate buffered saline, Sigma-Aldrich Chemie) as measured by OCCS yielded a mean diameter of 42.0 nm with a standard deviation of 4.7 nm (20 measurements lasting 20 seconds each; line rate of 50 kHz with an exposure time of $18\text{ }\mu\text{s}$; illumination power of 5 mW). These SPIONs were also measured with DLS (Malvern Zetasizer, using DTS Nano 7.02 software) and a mean diameter of 43.1 nm with a standard deviation of 13.5 nm was obtained (measured polydispersity index = 0.24). The mean values are in close agreement but the standard deviation is greater with DLS. The OCCS standard deviation was estimated with the different measurements, each based on approximately 1000 particle transits. In DLS the standard deviation is calculated on the NPs population directly.

The BSA at a neutral pH can be approximated as an equilateral triangular prism with sides of 8.4 nm and a height of 3.15 nm [33]. The hydrodynamic radius $R_H(N)$ of the SPIONs versus

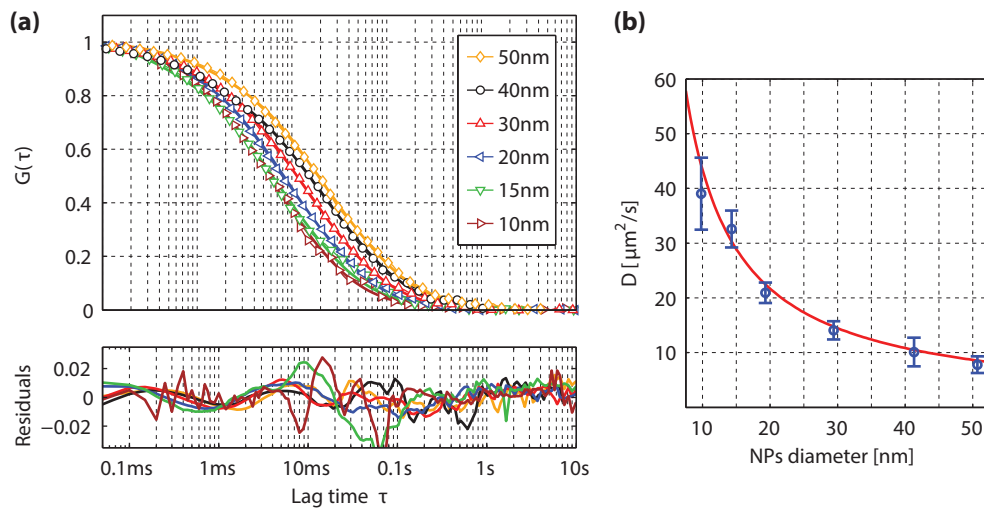


Fig. 5. (a) Normalized OCCS curves from gold NPs in V_0 of different diameters in glycerol/water solutions with 60% w/w of glycerol. Thin lines with markers show the average auto-correlations in V_0 of 10 measurements lasting 50 seconds each (line rate of 20 kHz with an exposure time of $48\text{ }\mu\text{s}$). Thick lines show the fits using Eq. (1) and the residuals. (b) The extracted diffusion coefficients from V_{-2} to V_2 matched well with the theoretical values.

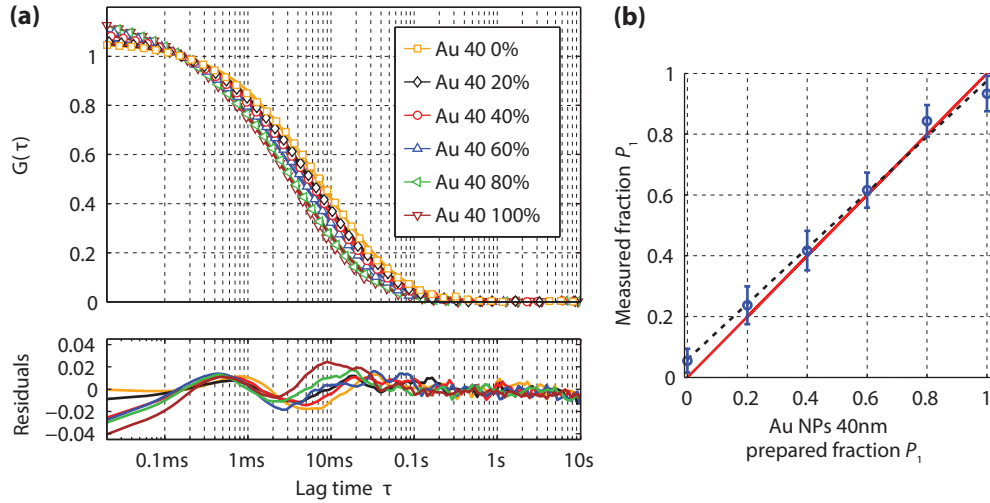


Fig. 6. OCCS of mixtures with two particle species. (a) Normalized OCCS auto-correlation curves from mixtures with different fractions of $\varnothing 40$ nm gold NPs and $\varnothing 109$ nm PS MSs in V_0 . Thin lines with markers show the average auto-correlations in V_0 of 10 measurements lasting 20 seconds each (line rate of 50 kHz with an exposure time of 18 μ s; illumination power of 5 mW). Thick lines show the fits using Eq. (2) and the residuals. (b) The measured fraction of the species \bar{P}_1 versus the mixed fraction P_1 . The red line represents the prepared values. The dotted black line is the linear regression of the measured \bar{P}_1 .

the number N of adsorbed proteins can be described by

$$R_H(N) = R_H(0) \sqrt[3]{1 + cN}, \quad (5)$$

where $c = V_p/V_b$ is the ratio of the volume V_p of the protein and the volume V_b of the bare NP [13]. The SPIONs $R_H(0) = 21.0$ nm yields $V_b = 38800$ nm³. Estimating the molecular volume of BSA from the size of the triangular prism we obtain $V_p = 96$ nm³ and hence $c = 2.5 \cdot 10^{-3}$. The measurements were performed for 330 pM SPIONs in PBS buffer solutions containing BSA concentrations ranging from 330 nM to 33 μ M (20 measurements lasting 20 seconds each; line rate of 50 kHz with an exposure time of 18 μ s; illumination power of 5 mW). Figure 7(a) shows the average OCCS auto-correlation curves in V_0 for measurements of solutions with 3.3 μ M BSA and without BSA. Figure 7(c) shows the distribution of the hydrodynamic radius that has been calculated for every sampling volumes ranging from V_{-2} to V_2 on the measurements with 3.3 μ M BSA and without BSA along with a fitted normal distribution. The difference between the extracted mean values of the distributions is $\Delta R = 3.1$ nm, suggesting that BSA molecules form a monolayer with their larger face on the SPIONs surface.

Using Eq. (5), the maximum number of adsorbed proteins N_{\max} is about 194 for the observed increase of R_H by 3.1 nm. For comparison, the coverage of the surface of a sphere with radius $R_H(0)$ would require about 181 BSA molecules which is in good agreement with N_{\max} and further indicates the formation of a monolayer. Figure 7(b) shows the hydrodynamic radii of the NPs as a function of BSA concentration. The standard deviations are mainly due to the polydispersity of the SPIONs. Following the approach by Rocker et al. [13], the experimental

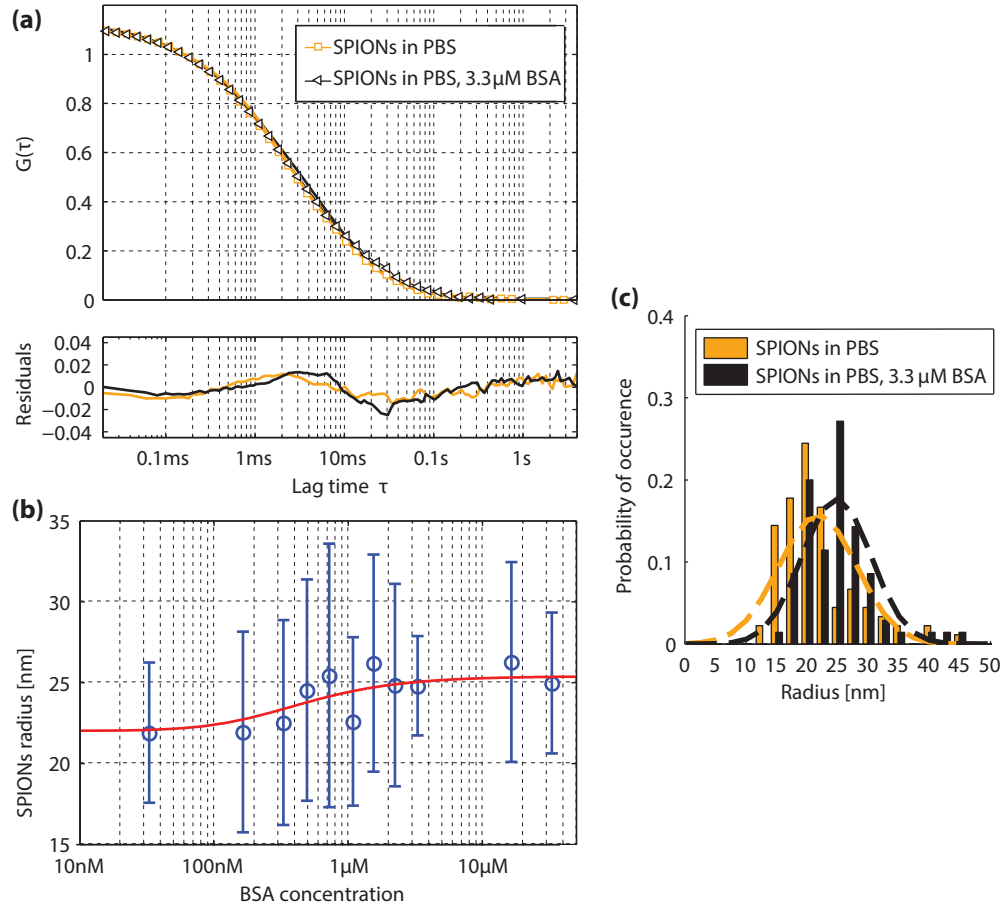


Fig. 7. Adsorption of BSA on SPIONs. (a) Normalized OCCS auto-correlation curves in V_0 of SPIONs 330 pM with 3.3 μM BSA and without BSA. Thin lines with markers show the average auto-correlations in V_0 of 20 measurements lasting 20 seconds each (line rate of 50 kHz with an exposure time of 18 μs ; illumination power of 5 mW). Thick lines show the fitting results using Eq. (1) and the residuals. The extracted hydrodynamic radii were $R_H = 21.4$ nm without BSA and 22.5 nm with BSA. (b) The hydrodynamic radii of the NPs versus BSA concentration. The thick red line corresponds to a fit with Eq. (5). (c) Distribution of hydrodynamic radii extracted from V_{-2} to V_2 of the auto-correlations.

data is fitted to a modified Langmuir model:

$$N = N_{\max} \frac{1}{1 + (K'_D / \langle C_{\text{BSA}} \rangle)^h}, \quad (6)$$

where N_{\max} is the maximum number of proteins binding to the nanoparticle, $\langle C_{\text{BSA}} \rangle$ is the average concentration of BSA, h is the Hill coefficient, and K'_D is the dissociation coefficient, which quantifies the strength of the protein–NP interaction. The fit of the data gives a trend line, however the standard deviation of the Hill coefficient is rather elevated, which does not allow a definite statement on the cooperativeness of the BSA adsorption.

We observed a full coverage above approximately 3.3 μM BSA concentration. Using this result, we can estimate the maximal concentration of SPIONs in serum for achieving full coverage by serum albumin. The reference range for albumin concentrations in serum is approximately 35–50 mg/ml [34]. By taking the lower bound of 35 mg/ml (corresponding to 526 μM), the maximal concentration of SPIONs in serum for a full coverage is estimated at 53 nM.

4. Conclusions

In comparison to the previous OCCS instrument working in the near-infrared wavelength range, we present an increase of the SNR by a factor of more than 25 with this visible light OCCS instrument. This improved SNR allowed the measurement of the diffusion coefficient of gold NPs down to a size of 10 nm diameter. The generalization of the fitting model to multiple component solutions has been applied to the measurement of the fractions of a mixture containing two different NPs species. For two NPs species with large difference in size (2.7:1) but similar brightness (1.2:1), we obtained excellent agreement of the measured fractions versus the prepared fractions. The measurement uncertainty and absolute error were small enough to qualify for an unambiguous distinction of the two NPs species.

We also measured the protein adsorption and formation of a protein monolayer on SPIONs, i.e. a study of the protein corona on NPs. These adsorption measurements were performed under physiological conditions using an intrinsic signal from the SPIONs, thus preventing potential modifications of these NPs that can occur when using fluorescent labels or separation steps. This achievement opens the door to the study of adsorption of other proteins of interest on SPIONs, in particular to the study of protein adsorption in serum.

In summary, the OCCS technique has been substantially enhanced and first applications highlight its potential for nanoscience and life sciences.

Acknowledgments

We acknowledge funding by the Swiss National Foundation (grant 205321L_135353) and support by the COST action MP1302 "NanoSpectroscopy".